Localization and Segmentation of Aortic Endografts Using Marker Detection

Marleen de Bruijne*, Wiro J. Niessen, *Associate Member, IEEE*, J. B. Antoine Maintz, and Max A. Viergever, *Member, IEEE*

***Abstract*—A method for localization and segmentation of bifurcated aortic endografts in computed tomographic angiography (CTA) images is presented. The graft position is determined by detecting radiopaque markers sewn on the outside of the graft. The user indicates the first and the last marker, whereupon the remaining markers are automatically detected. This is achieved by first detecting marker-like structures through second-order scaled derivative analysis, which is combined with prior knowledge of graft shape and marker configuration. The identified marker centers approximate the graft sides and, derived from these, the central axis. The graft boundary is determined by maximizing the local gradient in the radial direction along a deformable contour passing through both sides. Three segmentation methods were tested. The first performs graft contour detection in the initial CT-slices, the second in slices that were reformatted to be orthogonal to the approximated graft axis, and the third uses the segmentation from the second method to find a more reliable approximation of the axis and subsequently performs contour detection. The methods have been applied to ten CTA images and the results were compared to manual marker indication by one observer and region growing aided segmentation by three observers. Out of a total of 266 markers, 262 were detected. Adequate approximations of the graft sides were obtained in all cases. The best segmentation results were obtained using a second iteration orthogonal to the axis determined from the first segmentation, yielding an average relative volume of overlap with the expert segmentations of 92%, while the interexpert reproducibility is 95%. The averaged difference in volume measured by the automated method and by the experts equals the difference among the experts: 3.5%.**

***Index Terms*—Blood vessels, boundary detection, CTA, image segmentation.**

I. Introduction

An abdominal aortic aneurysm (AAA) is an enlargement of the infrarenal abdominal aorta, resulting from weakened arterial walls. Once present, AAAs continue to enlarge and, if left untreated, become increasingly susceptible to rupture, usually resulting in death. In conventional AAA treatment, the diseased part of the vessel is replaced by a synthetic graft during open surgery. This invasive procedure has serious drawbacks, including high mortality and complication rates and long hospital stays.

Endovascular aneurysm repair (EAR) is the minimally invasive alternative to AAA treatment [1]. Under fluoroscopic guidance, an endograft is navigated through a small groin incision into the aorta, whereupon an attachment system consisting of a series of metal hooks is pressed into the vessel wall by means of balloon inflations. Despite initial success of the endovascular procedure, complications can arise in due course. The process of aneurysm shrinkage, ongoing aneurysmal disease, and damage or fatigue of graft material may result in leakage, graft migration, and kinking or buckling of the graft, which can subsequently cause rupture or occlusion. Frequent and careful patient follow-up is therefore required [2]–[4].

In our study, computed tomographic angiography (CTA) scans are made of each patient that has received an endograft, within three days after surgery. Follow-up scans are made every 1.5 to 12 months, depending on the state of the aneurysm. The standard follow-up procedure includes definition of the central lumen line, thus enabling accurate graft and aneurysm diameter measurements, and graft lumen segmentation for volume measurements [5]. A volume representation of the graft enables clear visualization of graft morphology, thus revealing, e.g., graft kinking or lengthening. Current practice in graft segmentation is thresholded three-dimensional (3-D) volume growing under expert supervision, in which the expert places seed points in the aorta and iliac arteries. All image slices must be inspected; additional seed points can be placed in falsely excluded areas, and spurious regions, often caused by calcifications or radiopaque markers, must be separated from the lumen manually. This procedure takes an experienced operator approximately 10 min.

Automated vessel segmentation methods often start with the definition of a central axis. A popular approach relies on multiscale image structure analysis, providing the likeliness that a voxel belongs to the axis of a tubular object together with the tube axis and an estimate of its width [6]–[11]. This can be used as a vessel enhancement filter for visualization purposes or serve as the basis for cost-minimizing central axis extraction [9], [12], [13] or region-based segmentation. These methods are able to cope with varying vessel width, but yield unreliable results in case the underlying assumption of tubular shape does not hold, for example, at bifurcations, in extremely tortuous vessels, or in the presence of image artifacts. Lorigo *et al.* [14] proposed a vessel segmentation scheme using a one-dimensional curve evolving in 3-D space, which is especially good at capturing

Manuscript received April 11, 2002; revised November 1, 2002. This work was supported by the Netherlands Organization for Scientific Research (NWO). The Associate Editor responsible for coordinating the review of this paper and recommending its publication was W. Higgins. *Asterisk indicates corresponding author*.

*M. de Bruijne is with the Image Sciences Institute, University Medical Center Utrecht, Room E.01.335, Heidelberglaan 100, 3584 CX Utrecht, The Netherlands, and also with the Institute of Information and Computing Sciences, Utrecht University, 3584 CX Utrecht, The Netherlands.

W. J. Niessen, and M. A. Viergever are with the Image Sciences Institute, University Medical Center Utrecht, 3584 CX Utrecht, The Netherlands.

J. B. A. Maintz is with the Institute of Information and Computing Sciences, Utrecht University, 3584 CX Utrecht, The Netherlands.

Digital Object Identifier 10.1109/TMI.2003.809081

small vessels. Wink *et al.* [15] described an automated central vessel axis extraction plus vessel border estimation based on ray propagation. For the boundary extraction, a similar, more robust approach based on mean shift analysis is described by Tek *et al.* [16]. Given an approximation of the vessel axis, Verdonck *et al.* [17] established the lumen boundary through dynamic programming in reformatted slices perpendicular to that axis.

To our knowledge, no previous research has concentrated on automated segmentation of aortic endografts. The problem is similar to the segmentation of preoperative AAA [15], [18]–[21], with graft metal induced bright streak artifacts and shadows as an additional complexity. Juhan *et al.* [19] proposed a geometric modeling scheme that allows for extraction of the bifurcation and iliac arteries in preoperative AAA data. This approach requires preprocessing in the form of supervised contour definition in each slice. Automated methods based on volume growing [18] and 3-D deformable modeling [20] have been applied successfully to segmentation of the aorta and its branching vessels, but were not able to adequately segment the aortic bifurcation and the tortuous iliac arteries. Subasic *et al.* [21] and Magee *et al.* [22] reported promising results on preoperative data using 3-D level-sets, but did not yet present an extensive evaluation.

In general, methods relying on image intensity without incorporating explicit shape knowledge would, in the presence of graft metal, encounter similar problems as the expert guided segmentation that is currently clinically used. In this paper, a scheme for localization and segmentation of endografts, based on automated detection of radiopaque markers, is presented. The central axis and approximate boundary location can be deduced from the markers, whereupon accurate graft delineation is achieved through contour cost minimization using dynamic programming, similar to [17]. The advantage of the explicit marker detection is that, once the marker locations are known, their artifacts can be accounted for during the segmentation procedure. This work is an extension and evaluation of [23].

This paper is organized as follows. In Section II, the methods for marker detection, graft localization, and graft segmentation are discussed. The results of the methods as applied to ten CTA scans are presented and compared to manual marker indication and lumen segmentation by three experts in Section III. Section IV provides conclusions and a discussion.

II. Methods

The graft segmentation procedure is preceded by a localization step, which is based on the automated detection of radiopaque markers that are sewn on the graft. Section II-A explains the graft geometry, marker configuration, and position in the image. Section II-B presents a method for the detection of markers and marker-like structures. The correct marker configuration and graft position are derived as in Section II-C. Section II-D describes the final graft segmentation process.

A. Description of the Graft

The type of endograft that is used in our study is the Ancure Endograft bifurcated graft, as shown in Fig. 1. Worldwide, more than 5000 of these grafts are placed each year. The markers on this graft are hollow platinum cylinders with a radius of 1 mm and a length ranging from 1.5 to 5 mm. In CT images, they appear as bright, slightly elongated structures. Markers are sewn at both sides along the length of the graft, at intervals of approximately 10 mm. Two additional markers are placed at the bifurcation. The number of markers varies with the graft length. Available graft lengths are 12 to 19 cm, with 1-cm increments. The diameter varies from 20 to 26 mm.

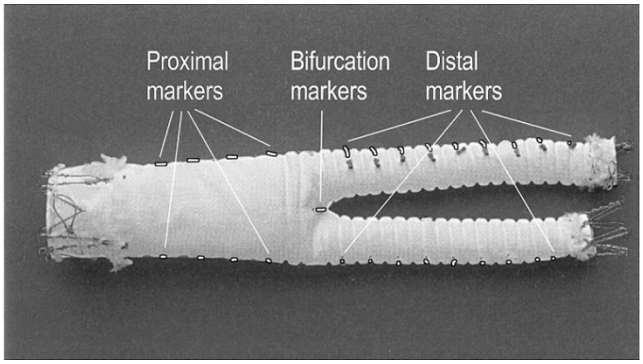

Fig. 1. Ancure Endograft bifurcated graft with the markers enhanced. Markers are sewn at regular intervals along the length of the graft, 180° apart. Two additional markers are placed in the bifurcation.

With respect to the graft cross-sectional shape in an image slice, we can distinguish three stages. While the contour of the graft starts out as a circular or oval shape near the proximal attachment, it gradually becomes more "8-shaped" when approaching the bifurcation. Beyond the bifurcation, two separate limbs are visible.

Following graft placement, the shape of the graft and its surrounding tissue can change considerably. The aneurysm sac generally shrinks when the pressure is released, as a consequence of which for instance calcifications that are distant from the lumen wall in the postoperative scans may be near the graft in a follow-up scan. In many patients, kinking or buckling of the graft has been observed [3].

B. Marker Detection

The markers are enhanced by means of a second-order derivative filter based on the eigenvalues of the Hessian matrix H [24] at a given voxel $\mathbf{x}$. $H(\mathbf{x})$ describes the local second-order structure in the original gray-valued image L

$$H(\mathbf{x}) = \begin{pmatrix} L_{xx}(\mathbf{x}) & L_{xy}(\mathbf{x}) & L_{xz}(\mathbf{x}) \\ L_{yx}(\mathbf{x}) & L_{yy}(\mathbf{x}) & L_{yz}(\mathbf{x}) \\ L_{zx}(\mathbf{x}) & L_{zy}(\mathbf{x}) & L_{zz}(\mathbf{x}) \end{pmatrix} \tag{1}$$

where subscripts denote derivatives to the corresponding spatial variables. Derivatives are computed by convolution with the derivative of a Gaussian kernel of width σ

$$\begin{aligned} L_{ij} &= L * \frac{\partial^2}{\partial i \partial j} G(\mathbf{x}, \sigma) \\ & i, j \in \{x, y, z\} \\ G(\mathbf{x}, \sigma) &= \frac{1}{\sqrt{2\pi\sigma^2}^3} e^{-\frac{\|\mathbf{x}\|^2}{2\sigma^2}}. \end{aligned} \tag{2}$$

We denote the eigenvalues of $H(\mathbf{x})$ by λ_1, λ_2, and λ_3, such that $|\lambda_1| \geq |\lambda_2| \geq |\lambda_3|$.

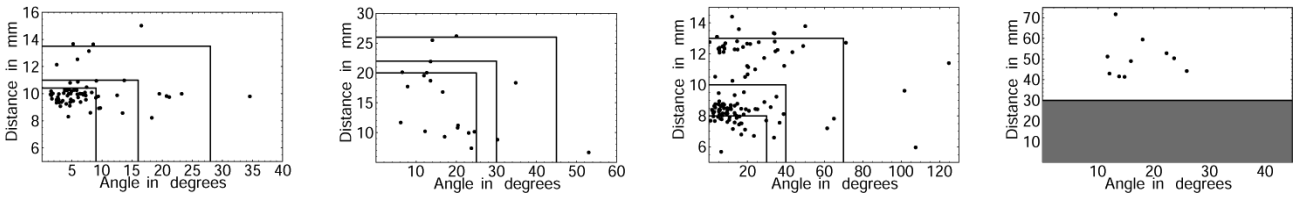

Fig. 2. Distances between successive markers and angles between line segments connecting successive markers, as measured in the (a) graft body, (b) bifurcation, and (c) limbs. (d) Distance from the proximal markers to the bifurcation markers, and the angle with the z axis. The lines denote search space boundaries.

Since the markers appear as bright cylinders, the local second-order structure at a marker voxel will reveal a strong negative second-order derivative in the directions perpendicular to the marker axis, and a weaker negative derivative along the axis. In terms of eigenvalues, this means $\lambda_1 \approx \lambda_2 < \lambda_3 < 0$. At small scales, $|\lambda_3|$ increases along the axis toward the marker endpoints, whereas at sufficiently large scales, the output of both endpoints coincides at the center. Thus, at appropriate scales, the marker center is associated with a local minimum in the product of the eigenvalues of the Hessian matrix.

A feature image containing the product of the eigenvalues of H at each voxel is computed. In this image, local minima that are formed by three negative eigenvalues correspond to the centers of bright blob-like structures in the original image and are potential marker centers. Local minima are detected by comparing the gray values in a 26-neighborhood for each voxel. A voxel is a local minimum if all of its 26 neighbors have higher gray values. If at least one of the neighbors has equal gray value and none is lower, the cluster of connected voxels with equal gray value forms a local minimum from which we select the center of gravity as the absolute local minimum. Local minima with low intensity in the original image $L(\mathbf{x}) < T$ are excluded. All remaining local minima are stored as potential marker centers, the product of eigenvalues representing their marker likeness.

C. Marker Selection

The set of potential marker coordinates resulting from the marker detection contains not only all markers, but also a small number of false positives. Additional information is needed to discern the true markers from other marker-resembling structures and to determine the proper ordering of markers along the graft. We propose an iterative tracking scheme, in which successive markers are searched at first in a small region. If no successor is found, the search region is enlarged and the process repeated.

1) Prior Knowledge: The search spaces are derived from ten CTA scans in which the markers are indicated manually. The distances between successive markers, the distance from the most proximal markers to the bifurcation markers, and the angles between the line segments connecting the markers were measured. These characteristics are different for the proximal and the distal part of the graft. The distances and angles measured are shown in Fig. 2. The distance between the bifurcation markers was 5.9±0.9 mm.

The size of the initial search space is set such that the average distance or angle plus one standard deviation is included, unless the chance of having two markers in that region would be large, in which case the first distance bound is kept smaller. The other search spaces comprise roughly 80%, 90%, and 100% of the markers. In this way, the chance of skipping one marker in the first search space is minimized, while outliers can be captured in the largest search space.

2) Tracking Algorithm: The graft localization algorithm consists of the following steps.

Initialization: The operator initializes the process by indicating the markers at the proximal and distal ends of the graft on both sides. The marker candidates that are nearest to the indicated points are selected as the end markers, thus limiting user dependency.

Bifurcation detection: Subsequently, the bifurcation markers are searched. All pairs m_1, m_2 of marker candidates in the bifurcation search space are evaluated. Bifurcation markers are close to each other, lie in the plane perpendicular to the graft axis, and are of the same size and orientation wherefore their marker likeness will be similar. The bifurcation pair must satisfy the following requirements:

$$3.2\,\text{mm} < |m_1 - m_2| < 8.6\,\text{mm},$$
$$|\text{angle}(m_1 - m_2, \text{z-axis})| \geq 45\,\text{deg}$$

and

$$\frac{\text{Min}\{f(m_1), f(m_2)\}}{\text{Max}\{f(m_1), f(m_2)\}} > 0.8$$

where $f(m)$ is the output of the Hessian filter. If more than one of these pairs exist, the pair nearest to the proximal markers is selected as the bifurcation pair.

Marker tracking: The tracking starts in vertical direction, downwards from the proximal end markers and upwards from the distal end markers, using the smallest search spaces. The strongest marker candidate in the search space is selected as the successor. The tracking continues from this marker along the direction from the previous marker to the current one.

Search space adaptation: If no suitable marker candidate was present, the process is repeated in a larger search space. The process stops if no successor was found even in the largest search space. When a new search space contains the bifurcation markers, it is adapted to bridge the gap between proximal and distal graft markers. Beyond the bifurcation, the search space is again adapted to account for the different properties of this part of the graft.

The algorithm terminates if no successors are found or the two lines on one side of the graft connect, i.e., when the end of the opposite line is encountered in the search space.

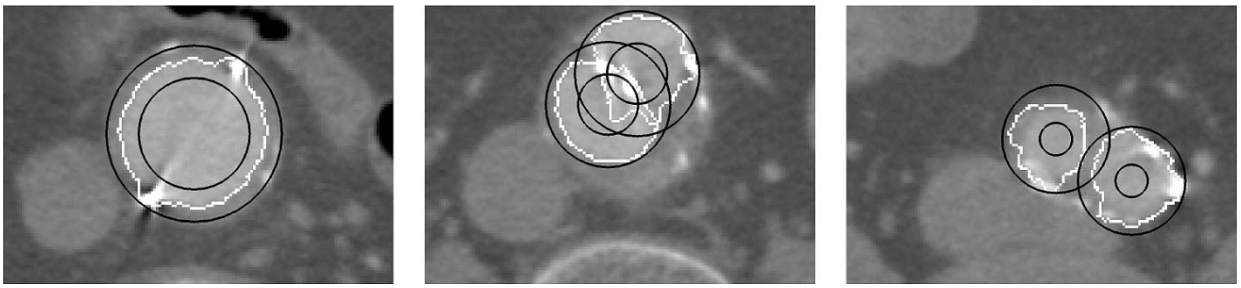

Fig. 3. Example CTA slices showing the boundaries of the polar image (black) and the contours detected (white) for, from left to right: the proximal part of the graft, just above the bifurcation, and the graft limbs. All CTA images in this paper have been contrast stretched for better visibility of the lumen.

D. Graft Segmentation

The marker locations confine the graft lumen and, hence, approximate the central lumen axis. In sequential image slices, the graft boundary is searched in a circular region comprising the approximate border location. Three approaches were tested.

1) The graft contour is detected in the original CT-slices (Section II-D1).
2) The graft contour is detected in reformatted slices orthogonal to the approximated central axis (Section II-D2).
3) As in (2), whereupon the central axis is determined from the contours obtained and a second iteration detects the boundary orthogonal to this axis (Section II-D-3).

1) Slice-Based Approach: Cubic B-spline interpolation between the markers defines two graft side points in each slice. The spatial average of those side points approximates the vessel center.

Polar images are constructed in each slice, showing the gray values along lines departing from the center point. The images are bounded by a minimum radius r_1 and a maximum radius r_2, defined as

$$r_1 = R - s_1 \tag{3}$$
$$r_2 = R + s_2 \tag{4}$$

where R denotes the obtained distance from the center to the graft side, and s_1 and s_2 are tunable parameters that allow for deviations from circular shape as well as some inaccuracy in the side point detection. Owing to the precise prediction of boundary location, the parameters s_1 and s_2 can be chosen small.

In the thus-constructed polar image, the edges in the tangential direction (t) are enhanced through convolution with the two-dimensional-scaled Gaussian derivative in radial direction (r)

$$L_r = L * \frac{\partial}{\partial r} G(\mathbf{x}, \sigma)$$
$$G(\mathbf{x}, \sigma) = \frac{1}{2\pi\sigma^2} e^{-\frac{\|\mathbf{x}\|^2}{2\sigma^2}}. \tag{5}$$

As the lumen is bright on a darker background, the lumen wall corresponds with a local minimum in the radial gradient. The optimal path through both established side points minimizing the radial gradient is obtained through dynamic programming; For a closed path, the minimum cost of all possible paths in the $m \times n$ polar image is given by

$$\mathrm{Min}_{r=r_1,r_m}\{C(t_n, r)\}$$

in which $C(t_n, r)$, the cost of a path starting at r, is obtained using

$$C(1, r) = L_r(1, r)$$
$$C(t+1, r) = \mathrm{Min}_{i=-1,0,1}\{C(t, r+i)\} + L_r(t+1, r). \tag{6}$$

The optimal path is determined by back tracking from the optimal endpoint.

Near the bifurcation the cross-sectional shape changes, and we can no longer assume that the graft boundary has minimal gradient in the radial direction at each point. At a distance d_{bif} proximal to the bifurcation markers, we therefore start searching for two smaller intersecting circles instead of one. The centers of these circles are interpolated between the center at d_{bif} and the approximated limb centers in the bifurcation. The confining radii r_1 and r_2 are again given by (3) and (4), where R is the distance to the graft side.

Beyond the bifurcation, for each limb only one side can be deduced from the markers, and the lumen center is estimated from the side point and the adjacent contour. If $\vec{p}$ and $\vec{q}$ are the side point and the obtained center in the previous slice, and $\vec{p'}$ is the side point in the next slice, then the approximate center $\vec{q'}$ in the next slice is given by

$$\vec{q'} = \vec{p'} + (\vec{q} - \vec{p}). \tag{7}$$

Since no accurate diameter is known beforehand, the polar image is bounded by fixed $r_{1_{\mathrm{distal}}}$ and $r_{2_{\mathrm{distal}}}$. Fig. 3 shows an example of the confined search region and the detected contour for each part of the graft.

A voxel representation of the graft lumen is constructed by flood filling the obtained contours.

2) Orthogonal to the Graft Axis and Sides: The central vessel axis is established as in Section II-D1. It is then resampled such that there is a sample point in each voxel the axis passes through. For each sample point, a polar image is constructed in the plane through the point and perpendicular to the axis. The images are bounded, and the contours searched, in the same way as in the slice-based approach. Beyond the bifurcation, the centers are estimated by

$$\vec{q'} = \vec{p'} + \mathbf{M}(\vec{q} - \vec{p}). \tag{8}$$

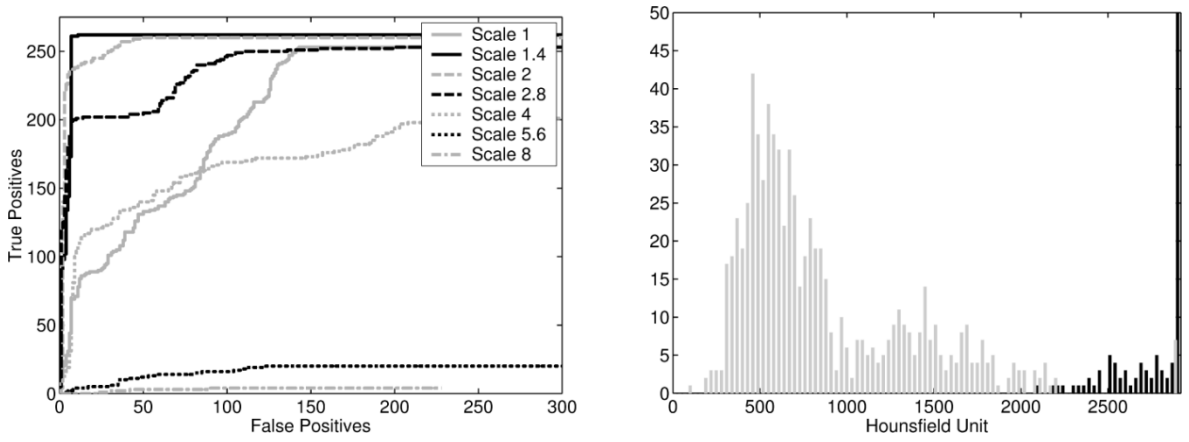

(a) (b)

Fig. 4. (a) ROC curve of markers detected in ten images at scales ranging from 1 to 8 mm. The total number of markers present in the images is 266, the maximum number detected is 262. (b) Histogram of gray values in the original image at marker candidate positions, for the false positives (gray) and true positives (black).

where $\mathbf{M}$ is the rotation matrix that maps the tangent at $\vec{p}$ onto the tangent at $\vec{p'}$. The polar images are constructed around the estimated center point but perpendicular to the graft side.

The result is an ordered set of nonparallel contours. Construction of a voxel representation is less straightforward than in the slice-based approach. Angular resampling, starting at the same marker line for each contour, results in contours with an equal number of points and known point correspondence. The graft surface is then approximated by a triangulation between successive contours. A slice can contain several intersecting contours, of which the outer envelope defines the graft wall.

3) Second Iteration Orthogonal to the Graft Axis: The central points of obtained contours define the central axis for the limbs, where previously only one side was known. A smooth central axis is obtained through cubic B-spline approximation, and the contour boundary detection as described in Section II-D1 is performed orthogonal to this curve.

E. Evaluation

The segmentations obtained are evaluated by means of visual inspection, computed overlap with expert segmentations, and agreement of measured volume with expert measurements.

The relative volume of overlap Ω of two volumes A and B is defined by

$$\Omega = 2\frac{|A \cap B|}{|A| + |B|}. \tag{9}$$

The averaged relative difference in measured volumes D for A with respect to B is defined as

$$D = 2\frac{|A| - |B|}{|A| + |B|}. \tag{10}$$

III. Experiments and Results

The three stages of graft segmentation as described in Section II, namely marker detection, marker selection, and three different approaches for graft boundary detection, are applied to ten CTA images. Since the automated procedure will have to cope with a relatively large deviation in graft postures and variations in the surrounding tissue, a diverse set of images is used, taken from different patients 0 to 48 months after graft placement, with graft lengths varying from 13 to 19 cm, and including kinked, rotated, and leaking grafts. The scan resolution is $0.488 \times 0.488 \times 2.0$ mm. The images consist of 121 to 171 slices of 512×512 voxels. Each image contains between 20 and 32 markers, depending on the length of the implanted graft. A total of 266 markers is present in the ten images. The computation time was about 1 min on a 1.70-GHz Pentium 4 PC for the marker enhancement filtering, and less than 10 s for the marker selection and graft segmentation together.

TABLE I
Parameters Used in all Experiments (mm), for Slice Based Approach (Method I) and the two Orthogonal Approaches (II and III)

	I	II/III	
s_1	6	4	Extent of search region inside markers
s_2	2	1	Extent of search region outside markers
d_{bif}	20	20	Size of bifurcation
$r1_{distal}$	3	3	Minimum limb radius
$r2_{distal}$	8	8	Maximum limb radius
σ	1	1	Width of Gaussian derivative kernel for edge detection

A. Marker Detection

The marker detection filter, with threshold $T = 0$, was applied at an exponential range of scales (seven ranging from 1 to 8 mm). The resulting potential markers were compared to the outcome of a manual marker detection strategy in which an operator points out the center of each marker in a multiplanar reformat facility. A marker candidate is considered a true marker if it lies within a 2-mm distance (the slice thickness) to one of the points indicated manually, and if that point has not yet been associated with another marker candidate. Otherwise, it is a false positive.

Fig. 4(a) shows the results for each scale, summed over all ten images, in a receiver operating characteristic (ROC) curve. Sorted by decreasing marker likeness, the number of markers detected correctly is plotted as a function of the number of false

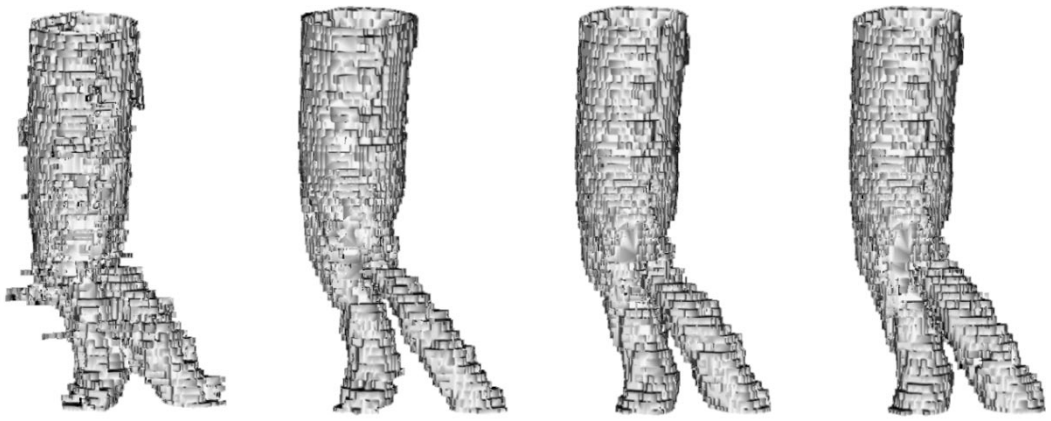

(a) (b) (c) (d)

Fig. 5. Volume representations of segmentations of the graft in dataset 3. From left to right, segmented by means of: (a) thresholded region growing under expert guidance, the current practice; (b–d) the proposed methods, slice-based (b), orthogonal to the axis and sides (c), and orthogonal to the axis using a second iteration (d).

positives. The area under a ROC curve measures the accuracy of the test, in this case its ability to distinguish between true markers and other bright blob-like structures present in the image. Clearly, the filter performs best at a scale of 1.4 mm, which is the size of the smallest markers. At smaller scales, many of the larger markers are detected as two separate smaller markers, of which one is counted as a false positive in our evaluation. At much larger scales, $\sigma \geq 4$ mm, two separate markers may be detected as one. At the optimum scale of 1.4 mm, 262 out of the total of 266 markers were detected, and six false positives were stronger than the weakest marker. Three of the cases in which a marker was not detected were caused by the two end markers, which were very close and hard to distinguish visually, being detected as one. In the fourth case, the marker was detected but at a distance of 2.3 mm from the point indicated manually, slightly over the allowed 2 mm. These errors will not hamper the use of the marker configuration as an initialization for graft segmentation.

The original gray value of the marker candidates is given in Fig. 4(b). Bone and calcifications cause false positives with an intensity of up to 1300 Hounsfield Units (HU), and graft metal up to 2300 HU. Another small peak at the maximum value (2895 HU) is caused by two parts of one marker being detected separately. Neither blob likeness nor original gray value can discriminate all true positives, but all bone and calcification induced false positives can be excluded by setting T at 1500. The remaining false positives are caused by graft metal. For robust marker identification and subsequent graft localization, it is important to use prior knowledge on graft geometry, as described in Section II-C.

B. Marker Selection

The marker selection scheme as described in Section II-C was applied to the set of marker candidates that were detected at the optimum scale of 1.4 mm. In all cases, our algorithm was able to find the bifurcation markers and track series of markers on the side of the graft, without including other marker-like structures. In seven out of ten scans, all markers were found. When during marker detection the two end markers were detected as one, naturally only one marker could be selected. In two scans, an additional marker was missed because two successive markers were both captured in one search space, and then only the strongest is selected. Yet, the graft sides could be properly estimated in all cases.

The exact positions indicated by the user are of negligible influence to the final graft approximation, provided that they are within a reasonably small distance, i.e., a few millimeters, to the true end marker position. As the marker candidate nearest to the indicated point is selected, even if that is not the intended end marker, it should be either another marker, causing the segmentation to be only shorter, or a part of the attachment system, which is also situated on the outside of the lumen and, thus, will not introduce a large error in the approximated graft side. In the ten scans of this study, the proper end markers were always found.

C. Graft Segmentation

The three methods for graft boundary detection are applied using parameter values as listed in Table I. These parameters are kept constant throughout the experiments, but could be adjusted if the scan protocol or the graft type changes. The robustness of the method with respect to parameter variations is discussed in Section III-C3. Sections III-C1 and Section III-C2 provide a quantitative evaluation of the final results.

One dataset could not be segmented using the slice-based approach since part of the graft was aligned in-plane, showing several successive markers in one slice. Segmenting orthogonal to the vessel axis was possible in this patient. Fig. 5 shows volume representations of the four different segmentations of one image. Although the automated approaches orthogonal to the axis yield subvoxel accurate segmentations, those have been transformed back to an anisotropic voxel representation to enable comparison with the expert segmentations.

The segmentations obtained by our method are smoother than the expert segmentation, mainly owing to marker-induced bright artifacts that are included in the region growing process that is used in the expert segmentation. Markers can also cause dark spots in the lumen, resulting in holes in the volume obtained by

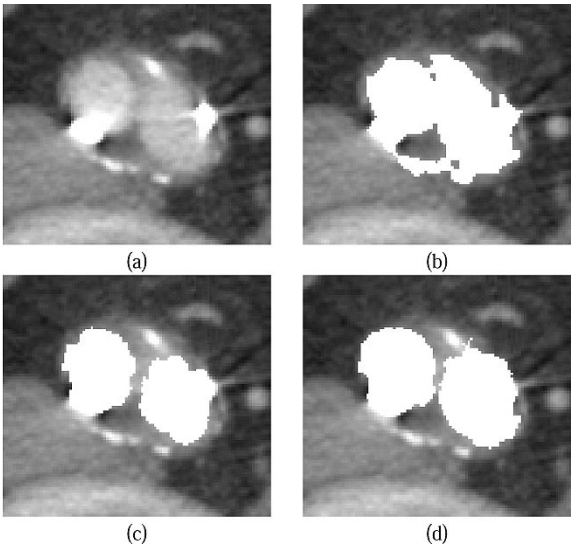

Fig. 6. Detail of a CTA slice below the graft bifurcation (a), segmented by region growing under expert guidance (b), the slice-based approach (c), and the approach orthogonal to the graft axis (d).

region growing. In addition, we observe that the automated procedures measure two separate limbs, while the expert segmentation tends to combine the limbs into one region. Cross-sectional images of the limbs in the original CTA image and in the segmentations are shown in Fig. 6. They reveal that the graft at that position indeed forms two separate lumens. Furthermore, the slice-based approach shows a slight undersegmentation of the graft limbs. This can be explained since the contour is searched in a limited circular region, while if the limbs are not parallel to the scan axis the in-slice contour can be quite elongated.

Fig. 7 provides projection images together with the detected markers and the center lines obtained by method III. The images show good results, even in grafts with severe kinking (first row), twisted limbs (second row), or a rotated graft body (third row).

1) Overlap: Table II lists the relative overlap Ω of the automated and expert segmentations for each scan, for the proximal and distal part separately. The last columns give the relative overlap for the entire graft. The results for the graft body show good agreement with the expert segmentation; the average volume of overlap is 94.3% and the minimum is 89.8%. For this part of the graft, the markers give a reliable approximation of the central axis and no second iteration is performed. There is no significant difference between the orthogonal and the slice-based approach; the proximal part of the graft is often virtually aligned with the scan axis and, therefore, the slice-based approach suffices.

Beyond the bifurcation, the method depending on the original CT-slices does not yield satisfactory results; the relative volume of overlap is 81.7% (min. 68.1%). This was anticipated as the underlying assumption that the graft contour is approximately circular does not hold when the lumen is oriented more parallel to the slice, which is often the case in the tortuous graft limbs. The results of the orthogonal approach are in better agreement with the expert segmentations—the overlap is 85.1% (min. 78.2). In particular, the worst results from method I, obtained for datasets 2, 3, and 5, have greatly improved. In those datasets, a second iteration orthogonal to the estimated central limb axis still increases the agreement with the expert segmentations. Still, the overlap is less than in the proximal part of the graft, 86.3% (min. 77.6%). This can be explained since in the distal part the expert segmentation is more influenced by the marker artifacts, as the markers are larger while the lumen is smaller. The relative volume of overlap for the entire graft is 92.0% (min. 86.8%) for the best of the three automated methods, and 95.1% (min. 92.1%) among the experts. Note, however, that the measure of overlap is biased toward segmentations that are obtained in a similar manner. A larger overlap does not necessarily imply better reproducibility of measurements.

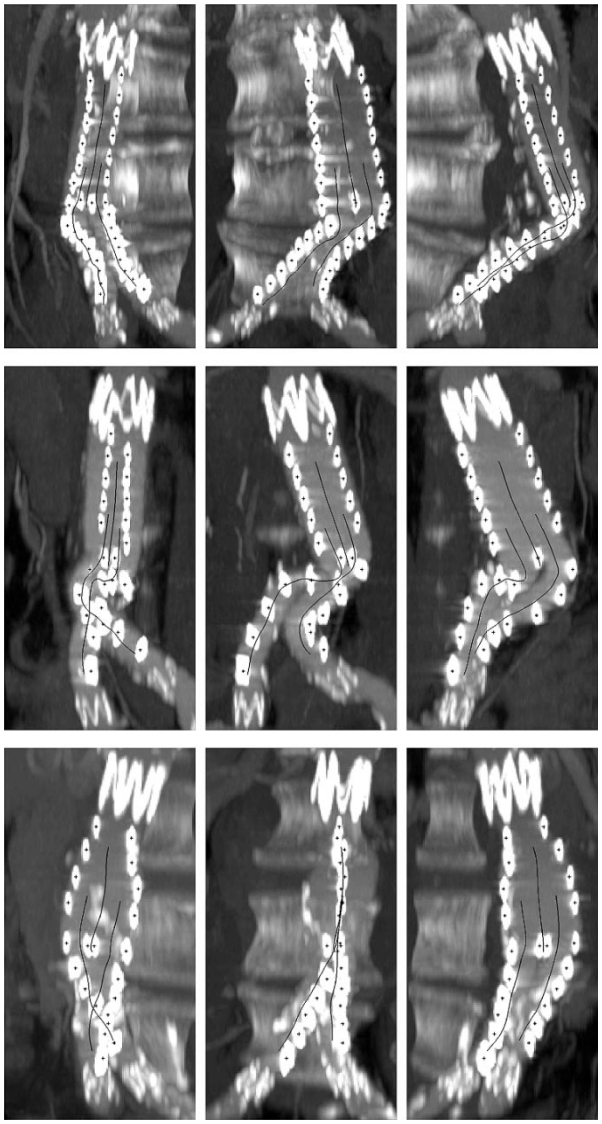

Fig. 7. Maximum intensity projection (MIP) images with the detected markers and detected central lines of graft body and limbs drawn in. The three rows show the results for three datasets; from top to bottom dataset 2, 5, and 8. The projections are made under different angles of rotation around the z axis; from left to right: $-60°$, $0°$, and $+60°$.

2) Volume Measurements: The clinically relevant quantity that is obtained from these segmentations is the lumen volume. Table III gives the relative difference in measured volumes D for the automated segmentations with respect to the expert segmentations, along with the differences between expert measurements.

TABLE II
RELATIVE VOLUME OF OVERLAP Ω (PERCENTAGE) AS COMPARED TO THE EXPERT SEGMENTATIONS, FOR METHODS I (SLICE-BASED), II (ORTHOGONAL), AND III (ORTHOGONAL USING A SECOND ITERATION), AND AMONG THE THREE EXPERTS

	Proximal			Distal				Total			
Dataset	I	II/III	Expert	I	II	III	Expert	I	II	III	Expert
1	92.6	90.6	98.0	87.9	84.9	83.8	94.6	91.0	88.6	88.2	96.9
2	95.2	95.3	97.2	68.6	81.5	86.1	93.0	89.1	91.7	92.8	96.0
3	94.7	95.3	96.4	71.2	84.4	86.9	92.3	92.5	94.2	94.4	95.9
4	94.0	93.6	93.6	81.9	88.7	88.6	89.4	89.7	91.7	91.7	92.1
5	-	96.2	97.5	-	78.9	85.1	88.6	-	90.9	92.7	93.5
6	93.9	91.8	96.3	78.7	82.2	81.3	89.8	88.7	88.4	88.0	94.5
7	96.1	96.6	96.7	86.9	89.7	90.0	92.3	92.9	94.1	94.1	95.7
8	95.8	95.4	97.2	86.4	89.0	89.2	92.4	93.9	94.0	94.0	95.3
9	94.9	93.7	96.3	88.7	90.2	90.1	91.6	92.2	92.2	92.1	95.9
10	95.1	94.8	96.6	85.1	81.5	82.1	90.3	93.0	92.0	92.1	95.2
Average	94.7	94.3	96.6	81.7	85.1	86.3	91.4	91.4	91.8	92.0	95.1
Min	92.0	89.8	93.6	68.1	78.2	77.6	88.6	87.9	87.1	86.8	92.1

TABLE III
AVERAGED ABSOLUTE VALUE $\langle |D| \rangle$, AVERAGED SIGNED VALUE $\langle D \rangle$ AND THE EXTREME VALUE OF THE VOLUME DIFFERENCE D BETWEEN THE AUTOMATED METHODS I–III AND THE EXPERT SEGMENTATIONS, AND AMONG EXPERTS (PERCENTAGE)

Method	$< \|D\| >$	$< D >$	extreme
I	3.4	-2.5	-7.0
II	3.4	0.9	9.2
III	3.5	0.14	9.6
Expert	3.5	-	7.8

No significant difference in measured volumes for method III and the expert segmentations was found. Assuming a t-distribution, the 95% confidence intervals for the relative volume difference were [−3.0,6.1], [−0.21,12], and [−7.9,−2.5] between the three experts and [−5.9,6.3], [−0.17,12], and [−6.4,4.9] for the automated method compared to the experts. The corresponding probabilities of zero mean difference were $p = 0.82$, $p = 0.062$, and $p = 0.0028$ between the experts and $p = 0.98$, $p = 0.062$, and $p = 0.82$ for the automated versus the expert measurements. The averaged absolute volume difference equals the interexpert difference: 3.5%.

3) Parameter Settings: The region in which the graft contour is searched is defined by the set of parameters s_1, s_2, d_{bif}, and $r_{2_{\text{distal}}}$ (see Table I). The search region should be as small as possible, to prevent tracing of the wrong edge, but large enough to ensure that the entire boundary is included. Examples of errors caused by bad parameter settings are shown in Fig. 8. Fig. 9 shows the effect of parameter variations on the false positive and false negative fraction for the final results of method III. The false positives are computed with respect to the union of the three manual segmentations, i.e., these voxels were labeled by the automated method but not by any of the three experts. The false negatives are the voxels that were consistently labeled as lumen by all three experts and not by our method. Note that false negatives include marker artifacts and calcifications that were erroneously included in the region growing process, while false positives include holes in the lumen caused by dark artifacts.

Naturally, if the search region excludes the true boundary, the errors become large. This can be the case for very small s_1, s_2, or $r_{2_{\text{distal}}}$, and for either small or large d_{bif}. The false negative fraction is robust to changes in s_1, but the false positives increase rapidly with increasing s_2 or $r_{2_{\text{distal}}}$. Outside the lumen more and stronger neighboring edges appear, which complicates graft boundary detection. This demonstrates the need for search space confinement as is done based on the marker locations. Satisfactory results were obtained for all datasets using the parameter values in Table I.

IV. CONCLUSION AND DISCUSSION

A method to localize and segment bifurcated aortic endografts in CTA scans is presented. The localization method is based on the automated detection of radiopaque graft markers using second-order derivative analysis combined with prior knowledge of graft and marker configuration. In ten scans, 262 out of a total of 266 markers were detected. Adequate approximations of both graft sides were obtained in all cases.

Three segmentation methods were tested. The first performs graft contour detection in the initial CT-slices, the second in reformatted slices orthogonal to the approximated graft axis, and the third uses the segmentation from the second method to find a more reliable approximation of the axis and subsequently performs contour detection.

For the proximal part of the graft, where the graft is still fairly straight and aligned with the body axis, all three methods yield similar results, in good agreement with the segmentations obtained by the experts. Beyond the bifurcation, performing contour detection orthogonal to the axis is needed to obtain satisfactory results in some patients. A second iteration orthogonal to the estimated central limb axis still increases the agreement with the expert segmentations. The relative volume of overlap for the entire graft is 92.0% (min. 86.8%) for the best of the three automated methods, and 95.1% (min. 92.1%) among the experts. No significant difference in measured volumes for method III and the expert segmentations was found. The averaged absolute volume difference equals the interexpert difference: 3.5%.

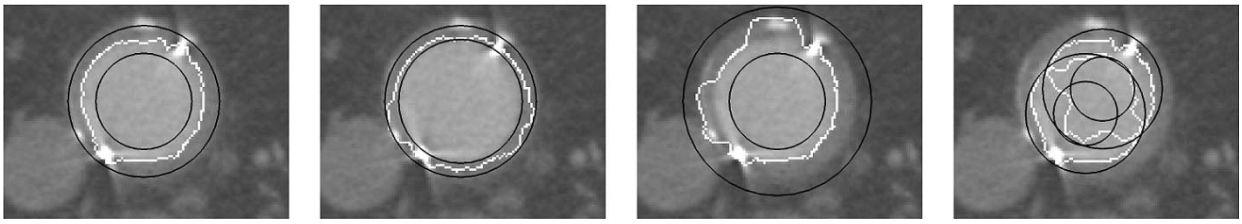

(a) (b) (c) (d)

Fig. 8. The effect of parameters s_1, s_2, and d_{bif}. (a) Correct segmentation, $s_1 = 4$ mm, $s_2 = 1$ mm. (b) Region too small, $s_1 = 1$ mm. The true boundary is outside the search region. (c) Region too large, $s_2 = 6$ mm. Neighboring boundaries are traced. (d) Region does not match cross-sectional shape, part of the true boundary lies outside the search region, $d_{\mathrm{bif}} = 60$ mm.

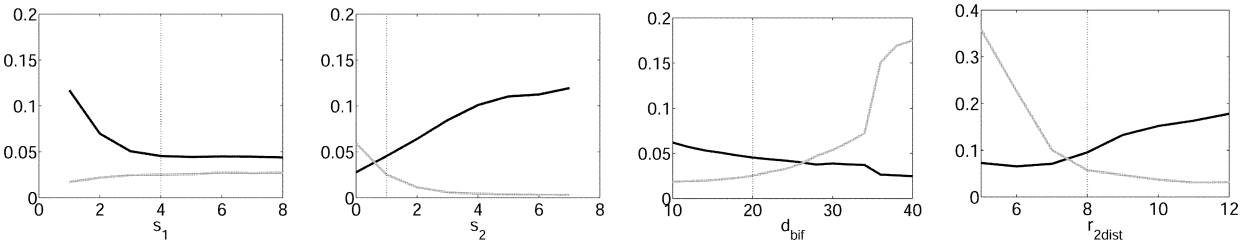

(a) (b) (c) (d)

Fig. 9. Average false positive fraction (black) and false negative fraction (gray) of the final results, as a function of the parameters. One parameter is varied while all others are kept fixed at the values listed in Table I and denoted by vertical lines in the plots. Fractions are computed with respect to the volume of the relevant graft part, i.e., the proximal part for figures (a)–(c) and the limbs for (d). (a) proximal inward deviation s_1. (b) Outward deviation s_2. (c) Bifurcation size d_{bif}. (d) Distal maximum radius $r_{2_{\mathrm{distal}}}$.

Our method can easily be extended to cope with other types of aortic endograft, viz. the tube graft and the monoiliac graft. For this study, we have chosen the bifurcated graft, since it is most commonly used and the most difficult to segment.

We have shown that, once the graft is precisely localized by the position of its markers, a fairly simple segmentation scheme can obtain good results. In future work, the method may be made more robust to variation in graft geometry by relaxing the bounds for the boundary tracing region and designing a cost function that is better able to distinguish between lumen and adjacent boundaries. Other possible applications for graft marker detection are the definition of a central lumen line for accurate diameter measurements, and performing graft curvature and torsion measurements.

ACKNOWLEDGMENT

The authors would like to thank their colleagues M.J. van der Laan, A. Teutelink, M. Prinssen, I.A.M.J. Broeders, and J.D. Blankensteijn from the Department of Vascular Surgery for many useful discussions, and for providing the datasets and expert segmentations.

REFERENCES

[1] J. Parodi, J. Palmaz, and H. Barone, "Transfemoral intraluminal graft implantation for abdominal aortic aneurysms," *Ann. Vasc. Surg.*, vol. 5, pp. 491–499, 1991.

[2] I. Broeders, J. Blankensteijn, A. Gvakharia, J. May, P. Bell, J. Swedenborg, J. Collin, and B. Eikelboom, "The efficacy of transfemoral endovascular aneurysm management: A study on size changes of the abdominal aorta during mid-term follow-up," *Eur. J. Vasc. Endovasc. Surg.*, vol. 14, no. 2, pp. 84–90, 1997.

[3] J. Wever, "CT angiographic follow-up after endovascular aortic aneurysm repair," Ph.D. dissertation, Utrecht Univ., Utrecht, The Netherlands, 1999.

[4] M. Fillinger, "Postoperative imaging after endovascular AAA repair," *Semin Vasc. Surg.*, vol. 12, no. 4, pp. 327–338, 1999.

[5] R. Balm, R. Kaatee, J. Blankensteijn, W. Mali, and B. Eikelboom, "CT-angiography of abdominal aortic aneurysms after transfemoral endovascular aneurysm management," *Eur. J. Vasc. Endovasc. Surg.*, vol. 12, no. 2, pp. 182–188, 1996.

[6] T. Koller, G. Gerig, G. Székely, and D. Dettwiler, "Multiscale detection of curvilinear structures in 2-D and 3-D image data," in *Proceedings of the Fifth International Conference on Computer Vision*, E. Grimson, S. Shafer, A. Blake, and K. Sugihara, Eds. Los Alamitos, CA: IEEE Comput. Soc. Press, 1995, pp. 864–869.

[7] C. Lorenz, I. Carlsen, T. Buzug, C. Fassnacht, and J. Weese, "A multi-scale line filter with automatic scale selection based on the Hessian matrix for medical image segmentation," in *Lecture Notes in Computer Science*, B. ter Haar Romeny, L. Florack, J. Koenderink, and M. Viergever, Eds. Berlin, Germany: Springer-Verlag, 1997, vol. 1252, Scale-Space Theory in Computer Vision, pp. 152–163.

[8] Y. Sato, S. Nakajima, N. Shiraga, H. Atsumi, S. Yoshida, T. Koller, G. Gerig, and R. Kikinis, "Three-dimensional multi-scale line filter for segmentation and visualization of curvilinear structures in medical images," *Med. Image Anal.*, vol. 2, no. 2, pp. 143–168, 1998.

[9] A. Frangi, W. Niessen, R. Hoogeveen, T. van Walsum, and M. Viergever, "Model-based quantitation of 3D magnetic resonance angiographic images," *IEEE Trans. Med. Imag.*, vol. 18, pp. 946–956, Oct. 1999.

[10] K. Krissian, G. Malandain, N. Ayache, R. Vaillant, and Y. Trousset, "Model-based detection of tubular structures in 3D images," *Comput. Vis. Image Understand.*, vol. 80, no. 2, pp. 130–171, 2000.

[11] S. Aylward and E. Bullitt, "Initialization, noise, singularities, and scale in height ridge traversal for tubular object centerline extraction," *IEEE Trans. Med. Imag.*, vol. 21, pp. 61–75, Feb. 2002.

[12] O. Wink, W. Niessen, B. Verdonck, and M. Viergever, "Vessel axis determination using wave front propagation analysis," in *Lecture Notes in Computer Science*, W. Niessen and M. Viergever, Eds. Berlin, Germany: Springer-Verlag, 2001, vol. 2208, Medical Imaging Computing & Computer-Assisted Intervention, pp. 845–853.

[13] F. Quek and C. Kirbas, "Vessel extraction in medical images by wave-propagation and traceback," *IEEE Trans. Med. Imag.*, vol. 20, pp. 117–231, Feb. 2001.

[14] L. Lorigo, O. Faugeras, W. Grimson, R. Keriven, R. Kikinis, A. Nabavi, and C.-F. Westin, "CURVES: Curve evolution for vessel segmentation," *Med. Image Anal.*, vol. 5, pp. 195–206, Mar. 2001.

[15] O. Wink, W. Niessen, and M. Viergever, "Fast delineation and visualization of vessels in 3-D angiographic images," *IEEE Trans. Med. Imag.*, vol. 19, pp. 337–346, Apr. 2000.

[16] H. Tek, D. Comaniciu, and J. Williams, "Vessel detection by mean shift-based ray propagation," in *IEEE Workshop on Mathematical Methods in Biomedical Image Analysis*, L. Staib and A. Rangarajan, Eds. Los Alamitos, CA: IEEE Comput. Soc. Press, 2001.

[17] B. Verdonck, I. Bloch, H. Maître, D. Vandermeulen, P. Suetens, and G. Marchal, "Accurate segmentation of blood vessels from 3D medical images," in *IEEE Int. Conf. Image Processing*, vol. 3, P. Delogne, Ed., Sept. 1996, pp. 311–314.

[18] M. Fiebich, M. Tomiak, R. Engelmann, J. McGilland, and K. Hoffman, "Computer assisted diagnosis in CT angiography of abdominal aortic aneurysms," in *Proceedings of SPIE*, K. Hanson, Ed. Bellingham, WA: SPIE, 1997, vol. 3034, Medical Imaging: Image Processing, pp. 86–94.

[19] V. Juhan, B. Nazarian, K. Malkani, R. Bulot, J. Bartoli, and J. Sequeira, "Geometrical modeling of abdominal aortic aneurysms," in *Lecture Notes in Computer Science*, J. Troccaz, E. Grimson, and R. Mösgez, Eds. Berlin, Germany: Springer, 1997, vol. 1205, Proceedings of Computer Vision, Virtual Reality and Robotics in Medicine and Medical Robotics and Computer-Assisted Surgery, pp. 243–252.

[20] A. Bulpitt and E. Berry, "Spiral CT of abdominal aneurysms: comparison of segmentation with an automatic 3D deformable model and interactive segmentation," in *Proceedings of SPIE*, K. Hanson, Ed. Bellingham, WA: SPIE, 1998, vol. 3338, Medical Imaging: Image Processing, pp. 938–946.

[21] M. Subasic, S. Loncaric, and E. Sorantin, "3D image analysis of abdominal aortic aneurysm," in *Proceedings of SPIE*, M. Sonka and K. Hanson, Eds. Bellingham, WA: SPIE, 2001, vol. 4322, Medical Imaging 2001: Image Processing, pp. 388–394.

[22] D. Magee, A. Bulpitt, and E. Berry, "Combining 3D deformable models and level set methods for the segmentation of abdominal aortic aneurysms," in *Proceedings of the 12th British Machine Vision Conference*, T. Cootes and C. Taylor, Eds: The British Machine Vision Association, 2001, pp. 119–126.

[23] M. de Bruijne, W. Niessen, J. Maintz, and M. Viergever, "Semi-automatic aortic endograft localization for post-operative evaluation of endovascular aneurysm treatment," in *Proceedings of SPIE*, M. Sonka and K. Hanson, Eds. Bellingham, WA: SPIE, 2001, vol. 4322, Medical Imaging 2001: Image Processing, pp. 395–406.

[24] T. Lindeberg, *Scale-Space Theory in Computer Vision*. Dordrecht, The Netherlands: Kluwer, 1994. The Kluwer International Series in Engineering and Computer Science.

[25] M. Sonka and K. Hanson, Eds., *Proceedings of SPIE*. Bellingham, WA: SPIE, 2001, vol. 4322, Medical Imaging: Image Processing.